NeuroImage 272 (2023) 120069

Contents lists available at ScienceDirect

NeuroImage

journal homepage: www.elsevier.com/locate/neuroimage

# White matter microstructure is associated with the precision of visual working memory

Xuqian Li[a,b,*], Dragan Rangelov[c], Jason B. Mattingley[c,d,e], Lena Oestreich[a,f], Delphine Lévy-Bencheton[a], Michael J. O'Sullivan[b,g]

[a] UQ Centre for Clinical Research, The University of Queensland, Brisbane, Australia
[b] Institute for Molecular Bioscience, The University of Queensland, Brisbane, Australia
[c] Queensland Brain Institute, The University of Queensland, Brisbane, Australia
[d] School of Psychology, The University of Queensland, Brisbane, Australia
[e] Canadian Institute for Advanced Research, Toronto, Canada
[f] Centre for Advanced Imaging, The University of Queensland, Brisbane, Australia
[g] Department of Neurology, Royal Brisbane and Women's Hospital, Brisbane, Australia

ARTICLE INFO

*Keywords:*
Visual working memory
Delayed estimation task
Mixture distribution modelling
White matter microstructure
Principal component analysis
Brain-behavior associations

ABSTRACT

Visual working memory is critical for goal-directed behavior as it maintains continuity between previous and current visual input. Functional neuroimaging studies have shown that visual working memory relies on communication between distributed brain regions, which implies an important role for long-range white matter connections in visual working memory performance. Here, we characterized the relationship between the microstructure of white matter association tracts and the precision of visual working memory representations. To that purpose, we devised a delayed estimation task which required participants to reproduce visual features along a continuous scale. A sample of 80 healthy adults performed the task and underwent diffusion-weighted MRI. We applied mixture distribution modelling to quantify the precision of working memory representations, swap errors, and guess rates, all of which contribute to observed responses. Latent components of microstructural properties in sets of anatomical tracts were identified by principal component analysis. We found an interdependency between fibre coherence in the bilateral superior longitudinal fasciculus (SLF) I, SLF II, and SLF III, on one hand, and the bilateral inferior fronto-occipital fasciculus (IFOF), on the other, in mediating the precision of visual working memory in a functionally specific manner. We also found that individual differences in axonal density in a network comprising the bilateral inferior longitudinal fasciculus (ILF) and SLF III and right SLF II, in combination with a supporting network located elsewhere in the brain, form a common system for visual working memory to modulate response precision, swap errors, and random guess rates.

## 1. Introduction

Visual working memory involves active maintenance and manipulation of visual information over a short period of time. It supports a range of cognitive functions and contributes to goal-directed behavior (Awh and Jonides, 2001; de Fockert et al., 2001; Gathercole et al., 2004; Henderson et al., 2014). Functional magnetic resonance imaging (fMRI) and positron emission tomography (PET) studies have shown that visual working memory relies on a widespread network of brain regions including the lateral prefrontal cortex, anterior insula, posterior parietal cortex, inferior temporal cortex, and early visual cortex (Daniel et al., 2016; Owen et al., 2005; Rottschy et al., 2012; Wager and Smith, 2003). Recent studies using network-based approaches have shown increased global efficiency and decreased modularity of functional networks during working memory compared with rest; these findings suggest that coordinated neural activity is required for working memory performance (Dagenbach, 2019). The idea that visual working memory relies on communication across a large-scale network implies a critical role for long-range white matter connections that support information transmission in the brain (Düzel et al., 2010; Pajevic et al., 2014). Here, we characterised the relationship between white matter microstructure and visual work-

* Corresponding author at: UQ Centre for Clinical Research, The University of Queensland, Building 71/918 RBWH Herston, Brisbane City QLD 4029, Australia.
*E-mail address:* xuqian.li@uq.edu.au (X. Li).

https://doi.org/10.1016/j.neuroimage.2023.120069.
Received 28 October 2022; Received in revised form 2 March 2023; Accepted 29 March 2023
Available online 30 March 2023.

ing memory performance in a large sample of neurotypical adult humans.

Previous studies have related visual working memory performance to white matter microstructure in several individual long-range association tracts (Lazar, 2017). In particular, the superior longitudinal fasciculus (SLF), a major pathway that connects the parietal and frontal lobes (Makris et al., 2005), has been related to visual working memory performance (Darki and Klingberg, 2015; Vestergaard et al., 2011). The SLF can be further divided into dorsal (SLF I), middle (SLF II), and ventral components (SLF III), which have different patterns of connectivity to other brain regions and, arguably, distinct functional specialization (Makris et al., 2005; Parlatini et al., 2017; Thiebaut de Schotten et al., 2011). Further, the inferior frontal-occipital fasciculus (IFOF), a tract that mediates direct communication between occipital and frontal lobes (Forkel et al., 2014), has also been associated with visual working memory (Krogsrud et al., 2018; Peters et al., 2014; Walsh et al., 2011). Finally, the inferior longitudinal fasciculus (ILF), a temporal-occipital tract that runs more superficially and ventrally than the IFOF (Herbet et al., 2018), also plays a role in modulating visual working memory function, based on evidence from healthy children and case studies of focal lesions (Krogsrud et al., 2018; Shinoura et al., 2007). Based on this existing literature, we focused on the relationship between visual working memory performance and five critical tracts-of-interest (TOIs): the SLF I, SLF II, SLF III, IFOF and ILF.

Conceptually, participant responses in visual working memory tasks can reflect true but noisy memory representations of target items, noisy representations of non-target items arising from feature binding failures (so-called “swap errors”), or random guesses originating from attentional lapses, poor task compliance or other factors. These specific aspects of visual working memory might be supported by totally different anatomical structures. Yet, research also suggests that the variabilities of memory representations and swap errors, for example, are affected by common neural factors such as the stochastic noise in the nervous system (Schneegans and Bays, 2017). It is therefore of great interest to know whether sources of variability in task responses are governed by distinct or shared white matter substrates. Unfortunately, previous investigations that aimed to relate visual working memory performance to white matter microstructure did not distinguish between sources of behavioral variability (Darki and Klingberg, 2015; Krogsrud et al., 2018; Nagy et al., 2004; Peters et al., 2014; Vestergaard et al., 2011; Walsh et al., 2011). The overarching goal of the current study was to use computational modelling of behavior to independently characterize contributions of white matter microstructure to these theoretically distinct components of visual working memory performance.

To evaluate visual working memory performance, we developed a novel version of the delayed estimation paradigm (Emrich et al., 2013; Gorgoraptis et al., 2011; Taylor and Bays, 2020), which required participants to encode three visual gratings that varied in both their spatial location and orientation. After a short delay period, participants reproduced, on a continuous scale, either the location or orientation of only one of the gratings, as indicated by a probe which appeared after the delay period. The different features to be retrieved (location and orientation) were included to test the extent to which brain-behavior associations are similar across the spatial and non-spatial domains of visual working memory. Having participants respond on a continuous scale allowed us to calculate error magnitudes that could be modelled using mixture distribution modelling to independently estimate *the precision* of “true” working memory responses, *the rates of swap errors*, and *the rates of random guessing* (Bays et al., 2009; Zhang and Luck, 2008). To avoid biasing results by selection of individual tracts or microstructural measures, while also reducing data dimensionality, we used a two-step principal component analysis (PCA) to estimate latent components over different *measures* and different *tracts*. The aim of this data-driven approach was to capture more holistic representations of white matter microstructure in long-range pathways, which helps explore patterns of brain-behavior association, or even interdependency between tracts, in shaping response precision, swap errors, and random guesses.

## 2. Methods

### 2.1. Participants

Eighty-seven healthy adult volunteers were recruited from The University of Queensland through an online volunteer system. Seven participants were excluded from subsequent analyses due to data corruption ($n = 4$) or incomplete MRI data ($n = 3$). The final sample included 80 participants aged from 18 to 38 years ($M = 24.24$, $SD = 4.61$; 39 females). All participants completed safety screening questionnaires and provided written informed consent before the experimental sessions. Participants were reimbursed at a rate of $20 per hour. The study was approved by the Human Research Ethics Committee of The University of Queensland.

### 2.2. Experiment

#### 2.2.1. Apparatus

Stimuli were displayed on an LCD monitor (VG248QE) with a resolution of 1920 × 1080 pixels and a refresh rate of 60 Hz. Participants were seated approximately 60 cm from the monitor in a dimly illuminated room, with their head position maintained with a chinrest. The experiment was implemented under MATLAB R2018a (MathWorks, Natick, MA) using Psychtoolbox (Brainard, 1997; Pelli, 1997). Eye position was recorded using a desk-mounted eye-tracking system sampled at 120 Hz (iView RED-m infrared eye tracker, SensoMotoric Instruments, Teltow, Germany). The eye-tracker was calibrated and validated before each experimental block using a five-point calibration grid. The experiment was performed concurrently with electroencephalography (EEG) recording but the EEG data are not reported in this manuscript.

#### 2.2.2. Visual working memory experiment

The location and orientation versions of the visual working memory tasks were presented in separate blocks in random order for each participant (Fig. 1). In each trial, participants were first presented with a black central cross (size: 1.32° in visual angle [dva]; RGB: 0, 0, 0; line thickness: 0.13 dva) and a black arrow (RGB: 0, 0, 0; width: 2.64 dva; height: 0.66 dva) located 2.64 dva above the fixation for 300 ms, reminding the participants to encode only items on the left or right side of the screen. The “Cue” display was followed by the “Encoding” display presented for 400 ms and comprising six orientated gratings (radius: 2.64 dva). The gratings were randomly arranged on an invisible circle (radius: 10.55 dva) with respect to their centre. Any two adjacent gratings were separated by at least 20° and maximally 90° center-to-center offset and no grating was presented within ±15° range from the vertical midline. The grating orientations were randomly sampled over a 0°–179° range in increments of 2° Following the encoding display, the “Maintenance” display appeared for 900 ms, comprising only the central fixation cross. Next, depending on the task, a “Probe” display showing either the location or orientation of one of the memorized gratings on the cued side was presented for 700 ms. Participants were instructed to maintain fixation until the “Response” display. If an eye movement or blink was detected, a trial was discarded and replayed at the end of the block.

For the location task, one of the memorized gratings on the cued side was presented in the center of the probe display. This probe item displayed the orientation of one of the three presented gratings on the cued side, independently of its location. Simultaneously with probe disappearance, a white response circle appeared in the “Response” display in the middle of the screen (radius: 10.55 dva; RGB: 255, 255, 255; line thickness: 0.13 dva). Participants reported the location of the target grating on the response circle using a computer mouse. At the beginning of the response display, the mouse cursor was set to the centre of the screen. Immediately after participants moved the cursor, a smaller black

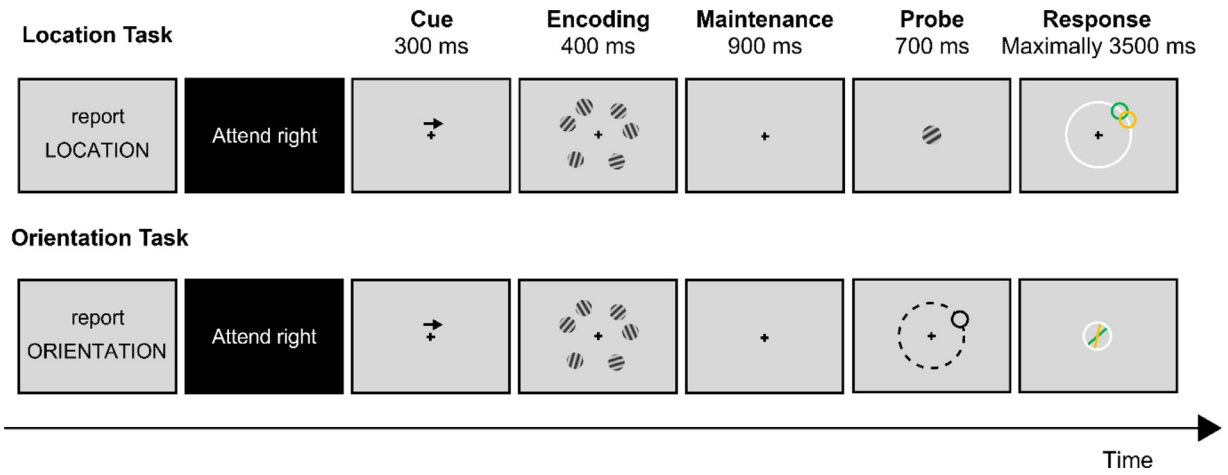


**Fig. 1.** Schematic Illustration of the Location and Orientation Tasks. At the start of each block, an instruction message appeared to indicate the subsequent task. At the beginning of each run, a message appeared on a black background to remind participants to encode items presented on either the left side or right side. In each trial, six gratings were presented during the encoding period. After a 900 ms delay period, participants provided a response based on the probe information.

circle (radius: 2.64 dva; RGB: 0, 0, 0) was revealed with a red dot (radius: 0.66 dva; RGB: 255, 0, 0) placed at its center. While moving the mouse, both circle and red dot were locked to the cursor movement to allow participants to adjust their response. A maximum of 3500 ms was set for the response period. Once a response was made, or at the end of the response period, a green feedback circle (radius: 2.64 dva; RGB: 0, 255, 0) representing the correct location of the probed item was shown for 1000 ms.

For the orientation task, a black circle outline (radius: 2.64 dva; RGB: 0, 0, 0) corresponding to the exact location of one of the three gratings on the cued side was presented in the probe display. This probe item displayed the spatial location of one of the three presented gratings on the cued side, independently of its orientation. Simultaneously with probe disappearance, a white response circle appeared in the "Response" display in the middle of the screen (radius: 2.64 dva; RGB: 255, 255, 255; line thickness: 0.13 dva). Participants reported the orientation of the target grating using the mouse. Similar to the location task, the mouse cursor was set to the center of the screen. As soon as participants started moving the cursor, a yellow line (RGB: 255, 255, 0; line thickness: 0.13 dva) inside the response circle was revealed and locked to the cursor movement. This helped the participants to adjust their response within a maximum response period of 3500 ms. Immediately following the response, or at the end of the response period, a green feedback line (RGB: 0, 255, 0; line thickness: 0.13 dva) representing the correct orientation was shown for 1000 ms.

Prior to the main experiment, all participants completed one practice block for each task with four trials per cued side (2 tasks × 2 cues × 4 trials = 16 trials). The main experiment consisted of four randomized blocks so that each of the tasks was presented twice. Each block contained two runs in which participants were cued to encode items on the left side of the screen, and two runs in which participants were cued to encode items on the right side, and these alternated with each other. The runs were counterbalanced across participants, with some participants always starting with right-side cues, and others with left-side cues. Each block comprised 120 trials, with 30 trials per run. A total of 480 trials were collected from each participant.

### 2.3. Behavioral analysis

To examine the quality of behavioral data, *response error magnitude* in each trial was computed as the angular difference between the participant's response and the objectively correct location or orientation of the cued item. The error magnitudes for the orientation task ranged between 0° and ±90°. In the location task, by contrast, the error magnitude ranged between 0° and ±180°, with errors larger than ±90° indicating that participants selected a location in the uncued hemifield. Initial data inspection indicated that participants never made such "hemifield-swap" errors, so subsequent analyses considered location in the same manner as orientation, with error magnitudes ranging between 0° and ±90°. For both tasks, the error magnitudes were transformed from degrees to pi radians ($\pi$rad) with 0° and ±90° mapped to 0 $\pi$rad and ±1 $\pi$rad, respectively. The error distribution for each participant was then compared against a uniform distribution using the Kolmogorov-Smirnov test (Massey, 1951). A uniform distribution would imply that a participant guessed in a majority of experimental trials. Based on this criterion, eight participants were excluded, leaving a total of 72 participants (36 females; 18–38 years; $M = 24.31$, $SD = 4.77$) for the following analyses.

To quantify performance on the task, a probabilistic model introduced by Bays et al. (2009) was applied, which attributes response error to a mixture of three components: (a) a von Mises distribution for the target orientation/location, (b) von Mises distributions for the non-target orientations/locations, and (c) a uniform distribution for random guesses. Technical details of this model have been described elsewhere (Bays et al., 2009). In brief, the model is defined as the probability of reporting the target item ($P_T$), the probability of reporting the non-target items ($P_{NT}$), the probability of random guessing ($P_G$), and the concentration parameter $\kappa$ of the von Mises distribution that described the variability around the target value. The non-target items in both the location and orientation tasks were defined as the two unprobed items presented on the cued side. The maximum likelihood estimates of the parameters were obtained separately for each participant in each task and cued side using an expectation-maximization algorithm. The fitted von Mises $\kappa$ was converted to circular standard deviation ($\sigma_{vM}$) as defined by Fisher (1995), giving a measure of *response precision* which reflects the precision of representations stored in visual working memory (Bays et al., 2011, 2011; Pratte et al., 2017). $P_{NT}$ measures *swap errors* which describe the proportion of responses arising from feature binding anomalies in working memory where a non-target feature is "swapped in" for the target feature (Bays, 2016; Schneegans and Bays, 2017). $P_G$ measures the *random guess rates* which reflect the proportion of responses originating from task-irrelevant factors.

A preliminary repeated-measures ANOVA on response precision, with task (location, orientation) and cued side (left, right) as the within-subject variables, showed no significant main effect of cued side and no significant interaction between task and cued side (all *ps* >> 0.05). Therefore, the mixture model was refitted to error distributions with trials aggregated across cued sides. Paired-samples *t*-tests were then performed to compare $\sigma_{vM}$, $P_{NT}$, and $P_G$ between the location and ori-

entation tasks. The mixture distribution modelling was performed in MATLAB R2020a using the Analogue Report Toolbox (Bays et al., 2009; Schneegans and Bays, 2016). All statistical analyses were carried out using R v4.1.0 (R Core Team, 2021).

### 2.4. Neuroimaging analysis

#### 2.4.1. Image acquisition

Participants underwent MRI scans using a Siemens Magnetom Prisma 3T system at the Centre for Advanced Imaging at The University of Queensland. T1-weighted structural scans were obtained with a magnetisation-prepared two rapid acquisition gradient echo (MP2RAGE) sequence (Marques et al., 2010), with 240 mm field-of-view (FoV), 176 slices, 0.9 mm isotropic resolution, TR = 4000 ms, TE = 2.92 ms, TI 1 = 700 ms, TI 2 = 2220 ms, first flip angle = 6°, second flip angle = 7°, and 5–6 min of acquisition time. Diffusion-weighted image (DWI) series were acquired using an echo-planar imaging (EPI) sequence with FoV of 244 mm, 70 slices, 2 mm isotropic resolution, slice acceleration factor = 2, TR = 4100 ms, TE = 84 ms. The acquisition consisted of 11 $b$ = 0 s/mm$^2$ ($B_0$) images, and 6, 10, 20, 60 diffusion-sensitization directions at $b$ = 200, 500, 1000, and 3000 s/mm$^2$, respectively. Additional 11 $B_0$ images were acquired with reverse phase encoding. The DWI sequence lasted approximately 7–8 min.

#### 2.4.2. Image processing

Image pre-processing was conducted using tools in MRtrix3 (v3.0_RC3; Tournier et al. 2019) and FSL (v6.0.4 FMRIB Software Library; Smith et al. 2004). T1-weighted images were brain extracted with the HD-BET algorithm, a new tool that has been validated on several large datasets and multiple MR sequences (Isensee and Hucho, 2019). DWI were denoised (Cordero-Grande et al., 2019; Veraart et al., 2016) and corrected for susceptibility induced field (Andersson et al., 2003), subject movement and eddy-current induced distortions (Andersson and Sotiropoulos, 2016), and signal intensity inhomogeneities (Zhang et al., 2001). A binary whole-brain masque was generated from the pre-processed DWI using the Brain Extraction Tool (BET; Smith, 2002). To achieve nonlinear registration from the native diffusion space to the MNI152 standard space, $B_0$ images were linearly registered to the respective T1-weighted images using rigid body transformation (Jenkinson et al., 2002) and the T1-weighted images were registered to the standard space using nonlinear registration (Andersson et al., 2007). The diffusion-to-T1 and T1-to-standard transformation matrices were concatenated and used to obtain the diffusion-to-standard warp fields.

The bi-tensor model as described in Pasternak et al. (2009) was used to obtain diffusion tensor measures including *fractional anisotropy* (FA), *mean diffusivity* (MD), *radial diffusivity* (RD), and *axial diffusivity* (AD) from the pre-processed DWI using $b \leq 1000$ s/mm$^2$ shells only, with the aim to minimize contamination of cerebrospinal fluid (CSF). To obtain more direct and specific markers of dendrites and axons, the neurite orientation dispersion and density imaging (NODDI) technique was also applied to the pre-processed multi-shell DWI using the NODDI MATLAB Toolbox (https://www.nitrc.org/projects/noddi_toolbox). This technique allows estimation of neurite density index (NDI), a measure likely to reflect density of dendrites or axons, and *orientation dispersion index* (ODI), a measure likely to reflect whether neurites are coherently orientated, along with estimation of a free water fraction by fitting a three-compartment tissue model to the diffusion signals (Zhang et al., 2012).

#### 2.4.3. Tractography and tractometry

The SLF I, SLF II, SLF III, IFOF, and ILF in both hemispheres were reconstructed according to a standardised protocol using automated probabilistic tractography as implemented in the XTRACT toolbox in FSL (Fig. 2; de Groot et al. 2013; Warrington et al. 2020). Anatomical landmarks use for fibre reconstruction are summarised in the Supplementary Methods. To guide tractography, a ball-and-stick, crossing-fibre model was applied to the pre-processed multi-shell DWI to estimate multiple fibre orientations in each voxel based on a continuous Gamma distribution of diffusivities (Jbabdi et al., 2012). Model parameters were estimated using a Bayesian Monte Carlo sampling technique. Probabilistic fibre tracking was then achieved by drawing sample streamlines from a seed along a diffusion orientation sampled from the posterior distribution at each voxel. A large number of samples built up a fibre probability distribution that reflected the number of streamlines connecting any single voxel to the seed masks (Behrens et al., 2007, 2003). All parameters that constrained streamline propagation were set as default: curvature threshold = ±80°, maximum streamline steps = 2000, step size = 0.5 mm (Warrington et al., 2020). The output normalized streamline density maps and average streamline length maps were used in the following analyses.

Along-tract profiling was performed for each TOI by mapping the microstructural measures with the average streamline length at each voxel. The average streamline length in a voxel for a given tract represents distance of streamline travelled from the seed region-of-interest (ROI) to that voxel, but this does not unambiguously distinguish all voxels when the seed ROI is placed in the middle of the tract trajectory since the measure of distance is non-directional. To add such directionality to the length maps of each TOI, the normalized density maps with a threshold at probability < 0.1% were masked to extract coronal slices anterior and posterior to the seed ROI, respectively. The resultant images were binarized to provide masks for the anterior and posterior segments of a tract which in turn, were applied to the average length maps. Distance values in voxels in the posterior segment of each tract was signed flipped to reflect direction of tract trajectory relative to the seed. The microstructural images were then mapped onto the corrected images of average streamline length. Finally, the streamline lengths were partitioned into 20 bins with a uniform width; the mean value of each microstructural measure was calculated for each bin of length to get an along-tract profile.

#### 2.4.4. Dimensionality reduction

For each participant, 6 microstructural measures were mapped along 200 regions (10 tracts × 20 length bins). To decrease data dimensionality, PCA was performed to identify principal components (PCs) over different measures and different tracts in a two-step fashion (Fig. 3). Previous studies have applied PCA either over different microstructural measures (Chamberland et al., 2019; Geeraert et al., 2020) or over different anatomical tracts (Clayden et al., 2012; Johnson et al., 2015; Penke et al., 2010). The two-step PCA combines the previously used approaches so that covariations along both the measure and tract dimensions can be captured effectively.

Two statistical tests were performed before each PCA to determine whether the data were suitable for structure detection. The Kaiser-Meyer-Olkin (KMO) Statistic measures the proportion of variance that might be caused by underlying factors. High KMO values generally suggest the suitability of applying PCA (Kaiser and Rice, 1974). A KMO value lower than 0.5 is considered to render PCA inappropriate (Dziuban and Shirkey, 1974). Bartlett's Test of Sphericity determines whether variables in a dataset are correlated; if all variables were unrelated, a PCA would be inappropriate (Bartlett, 1951). The above analyses were conducted using the 'REdaS' package (Maier, 2015).

The first PCA was performed on a concatenated data matrix with 6 columns (6 tissue measures) and 14,400 rows (72 participants × 10 tracts × 20 bins) to extract components from tissue measures. The second PCA was performed for each PC extracted from the first step by converting a data vector to a data matrix of 10 columns (10 tracts) and 1440 rows (72 participants × 20 bins), with the aim to further extract components from different tracts. To obtain PCA scores and loadings, singular value decomposition was applied to the mean-centered, $z$-transformed data matrix using the 'mdatools' package (Kucheryayskiy, 2020). PCs with eigenvalue > 1 were retained (Cattell, 1966). Loadings of the retained PCs were rotated using promax rotation to improve interpretability. Original tissue measures were considered to contribute substantially

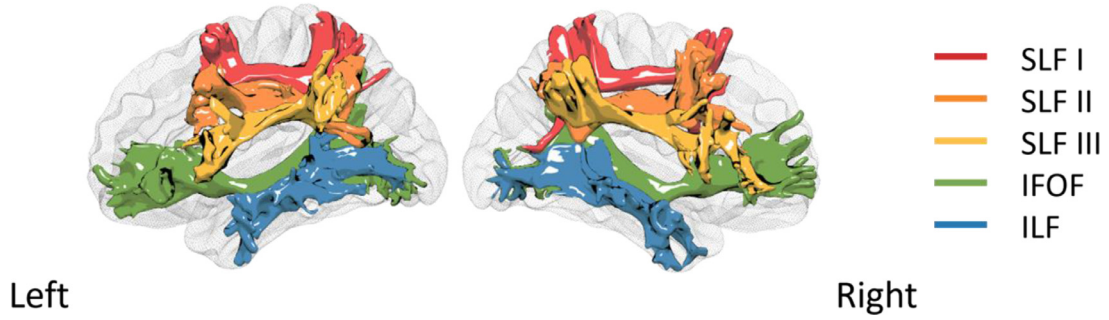


**Fig. 2.** Probabilistic Tractography of Ten Tracts of Interest. Normalised streamline density maps from a representative participant were applied with a threshold of 0.001, binarized, and converted to 3D meshes for the purpose of visualization. *Abbreviations*: SLF, superior longitudinal fasciculus; IFOF, inferior frontal-occipital fasciculus; ILF, inferior longitudinal fasciculus.

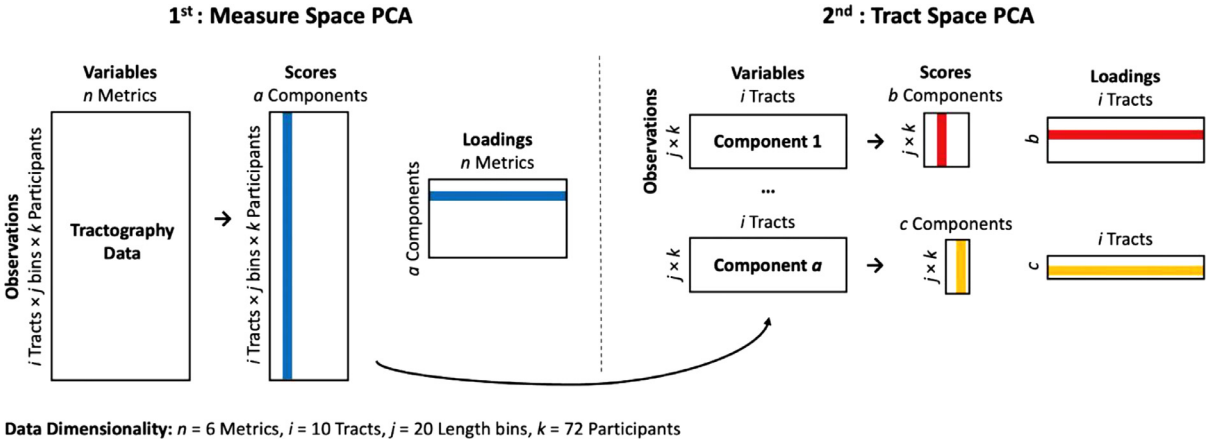


**Fig. 3.** Schematic Illustration of Two-step Principal Component Analysis (PCA). The measure space PCA aimed to capture covariations across 6 different microstructural metrics with 10 tracts × 20 length segments as observation for each of the 72 participants. Scores of the extracted components were then re-structured for the tract space PCA which captured covariations across 10 white matter tracts.

to a measure-space PC if they explained more variance than that would be equally explained by each variable (loading$^2$ > 1/number of variables). Original tracts were considered to have substantial contribution to a tract-space PC if the rotated loadings were above a 0.4 cut-off (Stevens, 2012; Yong and Pearce, 2013).

### 2.5. Statistical analysis

To examine brain-behavior relationships, linear mixed effects models were used to separately regress response precision ($\sigma_{vM}$), swap errors ($P_{NT}$), and random guess rates ($P_G$) on the identified PCs using R packages 'lme4' (Bates et al., 2015) and 'lmerTest' (Kuznetsova et al., 2017). PC scores for individual bins along tracts were averaged to produce a mean score per participant per PC for statistical analysis. To find the most parsimonious model that provided the best fit to the data, we adopted a step-up model building approach. This procedure starts with the construction of a base model, followed by the stepwise addition of predictor variables. Every new model is evaluated against a simpler model via the likelihood ratio test (LRT). In the present study, we tested fixed main effects of task (location vs. orientation) and all extracted PCs characterizing white matter connectivity as well as their interactions. In the case of significant interactions, the corresponding main effect terms were retained. Significant interactions were followed up using simple slope analysis as implemented in the 'reghelper' package (Hughes, 2021). Significance level was set at $p < 0.05$; $p$-values for fixed effects were calculated using Satterthwaite approximations. The above procedures were also repeated to explore effects of tract-specific PCs derived from the measure-space PCA (see Supplementary Results).

## 3. Results

### 3.1. Behavioral results

Distributions of error magnitudes were unimodal and centered on zero for both tasks (Fig. 4), indicating that participants were successful in reporting features of the target item. On average across participants, the estimated response precision was higher for the location task than for the orientation task ($\sigma_{vM}$ = 0.40/0.01 [M/SEM] vs. 0.74/0.03, $t(71) = -10.40$, $p < 0.001$). The estimated swap errors were higher for the location task than the orientation task ($P_{NT}$ = 0.34/0.01 vs. 0.03/0.01, $t(71) = -28.10$, $p < 0.001$). The estimated random guess rates were lower for the location task than the orientation task ($P_G$ = 0.02/ 0.01 vs. 0.36/0.03, $t(71) = 13.20$, $p < 0.001$).

### 3.2. Principal component analysis

The PCA over microstructural measures identified two PCs that collectively accounted for 89.5% of the variance (KMO: 0.58; Bartlett's Test: $\chi^2 = 486{,}752.48$, $p < 0.001$). The first component explained 67.3% of the variance, with FA and AD loading negatively while RD and ODI loading positively (Table S1). To facilitate interpretation, scores of $PC_1$ were multiplied by −1; higher scores on the first PC therefore represent increases in *fibre coherence*. The second PC explained 22.2% of the variance, with MD loading positively and NDI loading negatively (Table S1). Scores of the second PC were multiplied by −1; higher scores of therefore represent increases in *axonal density*.

Participant's scores of the extracted PCs from the measure-space PCA were next submitted to the tract-space PCA to capture covariance across

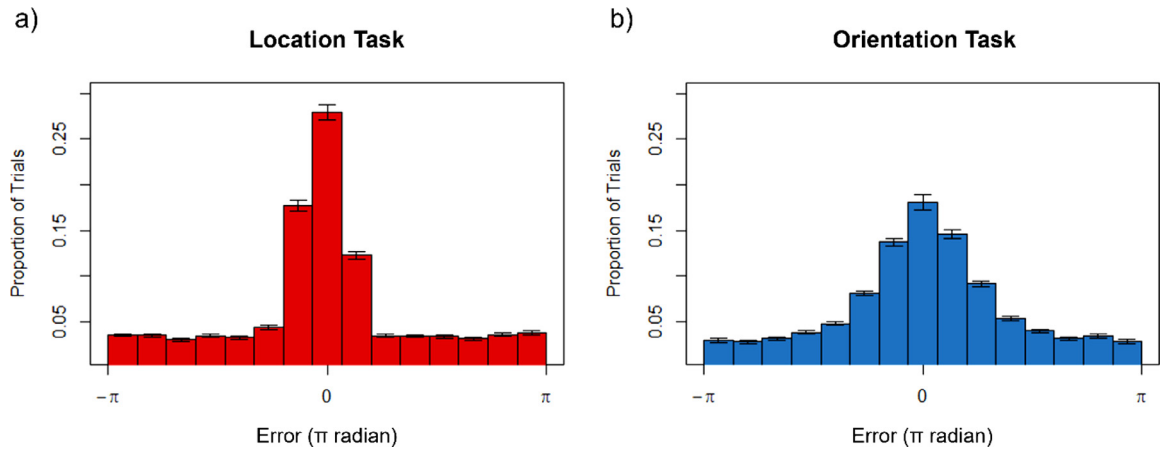


**Fig. 4.** Distributions of Response Errors in Visual Working Memory Tasks. Results of the (a) location task and (b) orientation task are shown. Proportion of trials within each bin is averaged across participants. Error bars in each bin denote standard errors of the mean.

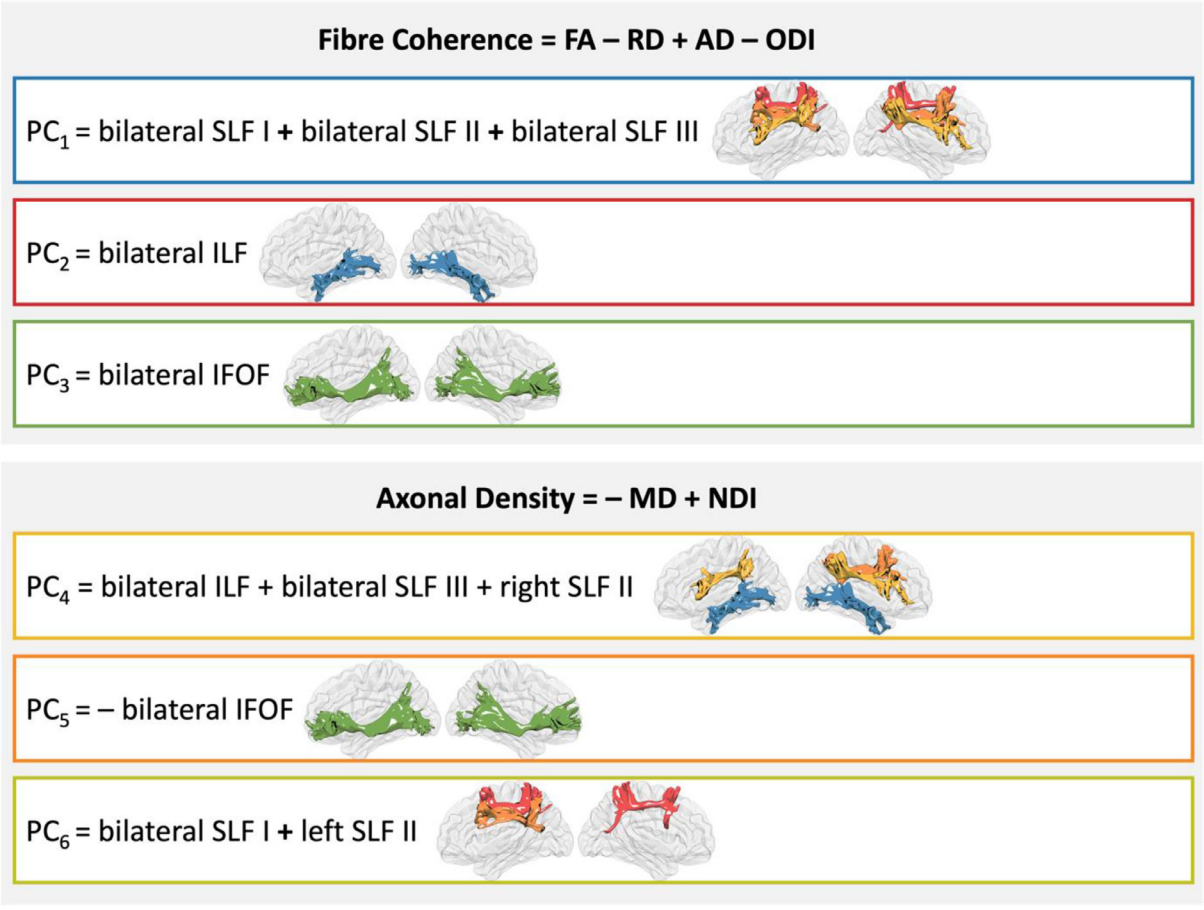


**Fig. 5.** Loading Profile of the Six Extracted Principal Components. *Abbreviations*: FA, fractional anisotropy; RD, radial diffusivity; AD, axial diffusivity; ODI, orientation dispersion index; MD, mean diffusivity; NDI, neurite density index; SLF, superior longitudinal fasciculus; IFOF, inferior frontal-occipital fasciculus; ILF, inferior longitudinal fasciculus.

TOIs. For fibre coherence, the tract-space PCA extracted three orthogonal PCs (eigenvalues > 1) which collectively explained 75.6% of the variance (KMO: 0.84; Bartlett's Test: $\chi^2 = 7715.13$, $p < 0.001$), and loaded onto three different groups of tracts (Fig. 5; Table S1). For axonal density, the tract-space PCA extracted three components that collectively explained 61.4% of the variance (KMO: 0.80; Bartlett's Test: $\chi^2 = 3811.15$, $p < 0.001$), which loaded onto three different groups of tracts (Fig. 5; Table S1). Biplots of the identified PCs are shown in Figs. S1 and S2. To summarize, six structural components were extracted from the high-dimensional tractography data.

### 3.3. Brain-behavior associations

The model comparison and selection processes for all dependant variables are summarized in Tables S2-S4. The best-fitting model of response precision showed a negative association between $\sigma_{vM}$ across

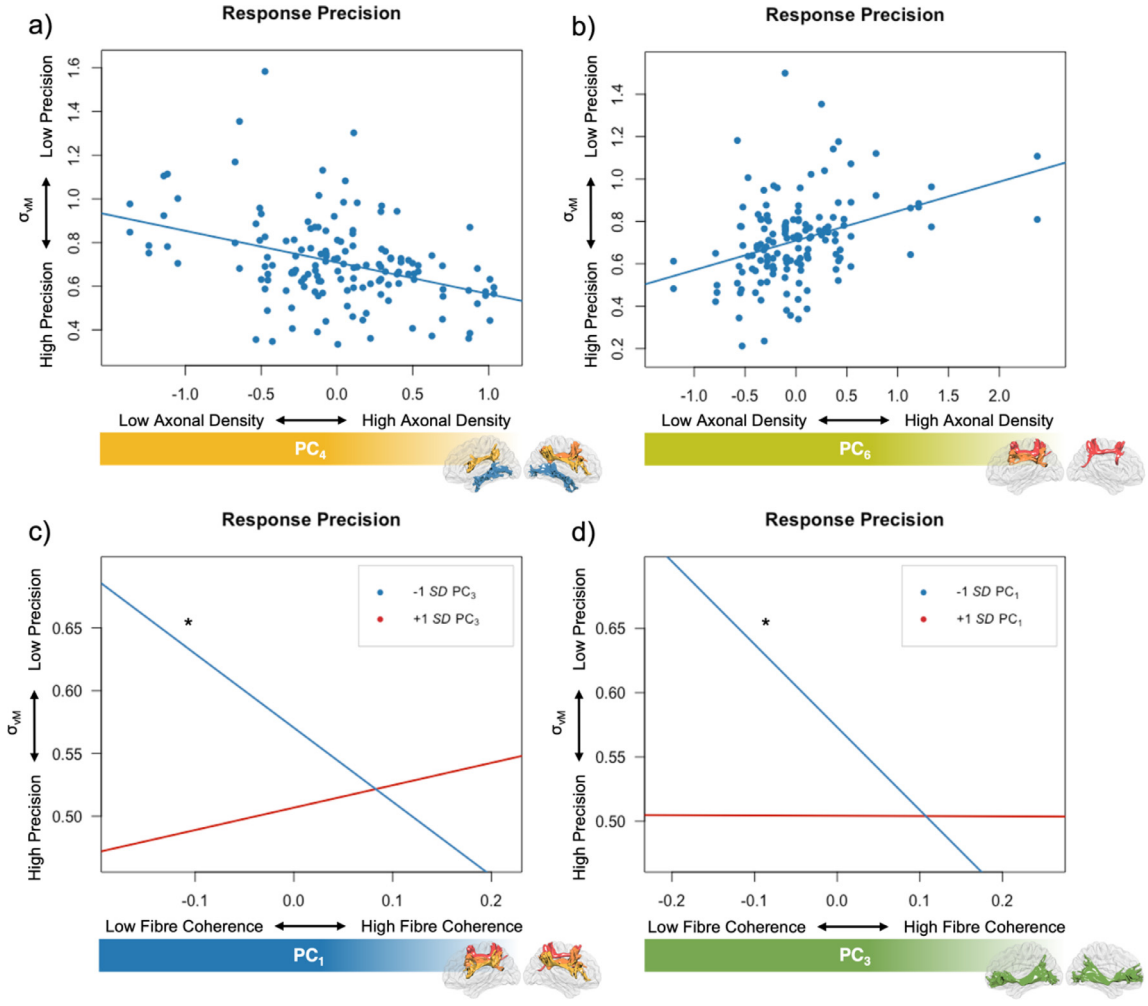


**Fig. 6.** Model of Response Precision. The regression plots show (a) the effect of $PC_4$ and (b) the effect of $PC_6$ on response precision as measured by $\sigma_{vM}$. Note that the plots show the partial effects of individual variables with other fixed effects and random effect in the linear mixed model partial out from the data. The interaction between $PC_1$ and $PC_3$ is plotted to show (c) the simple effects of $PC_1$ depending on the level of $PC_3$, and (d) the simple effects of $PC_3$ depending on the level of $PC_1$. Asterisks in plots (c) and (d) denote significant simple effects.

**Table 1**
The Best-fitting Model of Response Precision.

| Fixed Effects | Estimate | SE | *t* | 95% CI | *p* |
|---|---|---|---|---|---|
| Intercept (Orientation) | 0.71 | 0.02 | 29.21 | [0.66, 0.76] | < 0.001 |
| Task (Location) | -0.34 | 0.03 | -10.64 | [-0.40, -0.28] | < 0.001 |
| $PC_4$ | -0.14 | 0.05 | -2.76 | [-0.24, -0.05] | 0.007 |
| $PC_6$ | 0.14 | 0.04 | 3.11 | [0.05, 0.22] | 0.003 |
| $PC_1$ | -0.21 | 0.13 | -1.57 | [-0.45, 0.04] | 0.122 |
| $PC_3$ | -0.32 | 0.13 | -2.54 | [-0.57, -0.08] | 0.012 |
| $PC_1 \times PC_3$ | 1.92 | 0.54 | 3.58 | [0.90, 2.94] | 0.001 |
| Task × $PC_3$ | 0.33 | 0.16 | 2.05 | [0.02, 0.64] | 0.044 |

tasks and $PC_4$ (Fig. 6a; Table 1). This result indicates that higher axonal density in the bilateral ILF and SLF III and right SLF II was associated with lower $\sigma_{vM}$ and thus higher response precision in both the location and orientation tasks. There was also a significant association between $\sigma_{vM}$ across tasks and $PC_6$ (Fig. 6b); this result indicates that higher axonal density in the bilateral SLF I and left SLF II was associated with lower response precision in both tasks. In addition, there was a statistically significant interaction between $PC_1$ and $PC_3$ (Fig. 6c-d). This interaction was followed up with simple slope analyses. It was found that higher scores in $PC_1$ were associated with lower $\sigma_{vM}$ across tasks when $PC_3$ were low in scores ($p = 0.004$; Fig. 6c, blue line); this finding indicates that when fibre coherence was lower in the bilateral IFOF, higher fibre coherence in the bilateral SLFs I, II, and III was related to higher response precision in both tasks. When $PC_3$ were high in scores, however, there was no significant association between $PC_1$ and $\sigma_{vM}$ ($p = 0.195$; Fig. 6c, red line). Also, higher scores in $PC_3$ were associated with lower $\sigma_{vM}$ across tasks when $PC_1$ were low in scores ($p < 0.001$; Fig. 6d, blue line) and no significant association between $PC_3$ and $\sigma_{vM}$ when $PC_1$ were high in scores ($p = 0.987$; Fig. 6d, red line). A *post hoc* model including a three-way interaction among $PC_1$, $PC_3$, and task did not significantly improve the model fit, suggesting that the interaction between $PC_1$ and $PC_3$ did not differ between the location and orientation tasks (Tables S5 and S6). Finally, a significant interaction between task and $PC_3$ was found; the simple slope analysis revealed that higher fibre coherence in the bilateral IFOF was predictive of higher response precision only in the orientation task ($p = 0.012$).

The best-fitting model of swap errors revealed a negative association between $P_{NT}$ across tasks and $PC_4$ (Fig. 7a; Table 2); this indicates that higher axonal density in the bilateral ILF and SLF III and right SLF II was associated with lower swap errors in both the location and orientation tasks. There was also a significant association between $P_{NT}$ across tasks and $PC_6$ (Fig. 7b). This finding suggests that higher axonal density in the bilateral SLF I and left SLF II was associated with higher swap errors in both tasks.

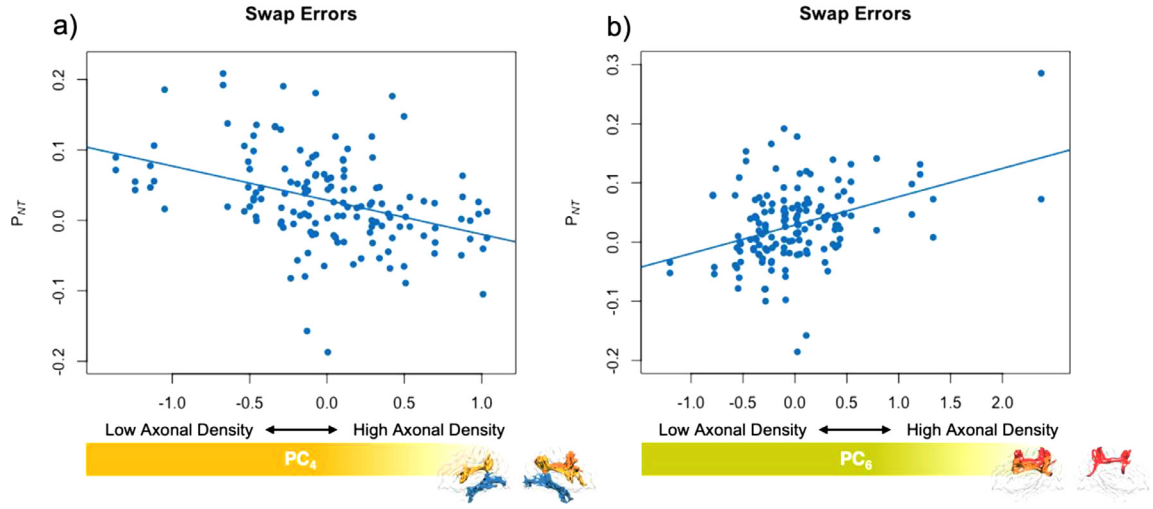


**Fig. 7.** Model of Swap Errors. The regression plots show (a) the effect of $PC_4$ and (b) the effect of $PC_6$ on swap errors. Note that the plots show the partial effects of individual variables with other fixed effects and random effect in the linear mixed model partial out from the data.

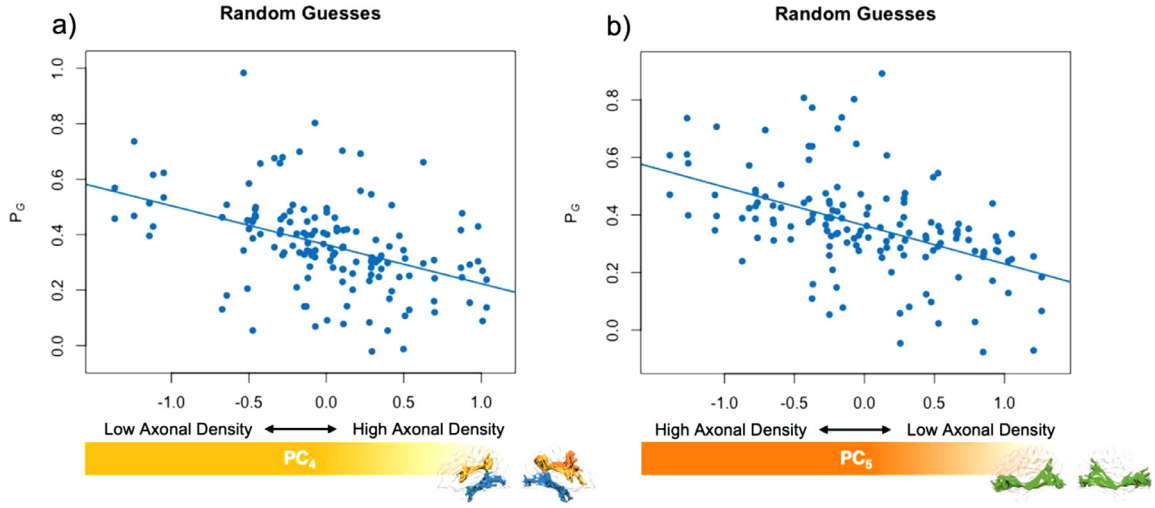


**Fig. 8.** Model of Random Guesses. The regression plots show (a) the effect of $PC_4$ and (b) the effect of $PC_5$ on random guesses. Note that higher values in $PC_5$ relate to lower extent of axonal density in the bilateral IFOF. The plots show the partial effects of individual variables with other fixed effects and random effect in the linear mixed model partial out from the data.

**Table 2**
The Best-fitting Model of Swap Errors.

| Fixed Effects | Estimate | SE | *t* | 95% CI | *p* |
|---|---|---|---|---|---|
| Intercept (Orientation) | 0.03 | 0.01 | 3.33 | [0.01, 0.05] | 0.001 |
| Task (Location) | 0.31 | 0.01 | 28.06 | [0.29, 0.33] | < 0.001 |
| $PC_4$ | -0.05 | 0.02 | -2.80 | [-0.08, -0.01] | 0.007 |
| $PC_6$ | 0.05 | 0.02 | 2.76 | [0.01, 0.08] | 0.007 |

**Table 3**
The Best-fitting Model of Random Guesses.

| Fixed Effects | Estimate | SE | *t* | 95% CI | *p* |
|---|---|---|---|---|---|
| Intercept (Orientation) | 0.36 | 0.02 | 19.62 | [0.33, 0.40] | < 0.001 |
| Task (Location) | -0.34 | 0.03 | -13.16 | [-0.39, -0.29] | < 0.001 |
| $PC_4$ | -0.14 | 0.05 | -3.01 | [-0.23, -0.05] | 0.004 |
| $PC_5$ | -0.13 | 0.04 | -3.44 | [-0.21, -0.06] | 0.001 |

The best-fitting model of random guess rates, again, revealed a negative association between $P_G$ across tasks and $PC_4$ (Fig. 8a; Table 3), suggesting that higher axonal density in the bilateral ILF and SLF III and right SLF II was associated with lower likelihood of guessing in both the location and orientation tasks. There was also a significant association between $P_G$ across tasks and $PC_5$ (Fig. 8b). This association suggests that higher axonal density in the bilateral IFOF was associated with more guesses in both tasks.

## 4. Discussion

The principal aim of the current study was to characterize the relationship between distinct aspects of visual working memory performance and the microstructure of major white matter tracts. Interdependency in fibre coherence between the bilateral SLFs I, II, and III and the bilateral IFOF mediated, in a functionally specific manner, participants' response precision. Axonal density in the bilateral SLF III and ILF and right SLF II, on the other hand, seems to be a common modulator for the precision of memory representations and errors arising from feature binding failures and random guesses.

In the best-fitting model of response precision, we found a significant interaction between $PC_1$ and $PC_3$. $PC_1$ represents fibre coherence in the bilateral SLFs I, II, and III, whereas $PC_3$ represents fibre coherence in the bilateral IFOF. We found that higher fibre coherence in the SLF bilater-

ally was associated with higher memory precision in both location and orientation tasks in participants with more dispersed fibres in the bilateral IFOF (Fig. 6b, blue line). It was also true that higher fibre coherence in the bilateral IFOF was associated with more precise responses when fibres in the bilateral SLF were less coherently orientated (Fig. 6c, blue line). The interaction between $PC_1$ and $PC_3$ further reveals an interdependence of SLFs I, II, III and IFOF when predicting response precision in visual working memory tasks. This observation suggests that individual differences in memory precision are modulated by an interplay between subsets of tracts that perhaps support distinct frontoparietal-occipital subnetworks. It is noteworthy that the models of swap errors and random guesses showed no effect of $PC_1$ and $PC_3$, suggesting that the fibre coherence in a frontoparietal-occipital network specifically mediates the precision of visual working memory, independently of errors arising from binding failures or poor task compliance. Previous studies have shown that higher FA and lower RD in both SLF and IFOF were associated with better performance in visuospatial working memory tasks (Darki and Klingberg, 2015; Nagy et al., 2004; Peters et al., 2014; Vestergaard et al., 2011; Walsh et al., 2011). Our result extends previous findings in two important ways. Firstly, by extracting components from both traditional tensor and NODDI metrics, we were able to bring current and previous findings together in a single conceptual framework of alterations in fibre coherence. Secondly, we were able to explore the interdependency between groups of tracts in shaping a specific aspect of behavioral response.

In addition to the brain-behavior associations specific to response precision, common white matter substrates for response precision and swap errors were also found. Higher scores on $PC_4$, that is, higher axonal density in bilateral ILF and SLF III and right SLF II, were associated with higher response precision and lower swap errors in both the location and orientation tasks (Fig. 6a, 7a). Also, lower scores on $PC_6$, describing *lower* axonal density in the bilateral SLF I and left SLF II, were found to be associated with a higher response precision and lower swap errors across tasks (Figs. 6b and 7b). These findings together suggest that a dual system might exist for modulating memory precision and feature binding efficiency, and this modulation is mainly achieved by regulating the amount of transmitted information which in turn, is mediated by levels of axonal density (Alexander et al., 2007, 2019; Beaulieu, 2002). Existing knowledge about other functions of the SLF III/ILF and SLF I supports this idea. In addition to visual working memory, cognitive processes like response inhibition, decision making, and visual guided behavior have also been implicated in SLF III and ILF (Herbet et al., 2018; Parlatini et al., 2017). These processes are closely related to the precision of memory representation and thus, it seems reasonable to allow more fine-grained information to transmit through this network when performing a visual working memory task. The SLF I, on the other hand, was associated with functions like saccades and mental imagery (Parlatini et al., 2017). It is possible when the primary goal is to maintain the memorised items, lower extent of axonal density in the SLF I is more beneficial regarding a lower extent of external or internal interference produced by these processes.

In the best-fitting model of random guesses, we found significant effects of $PC_4$ and $PC_5$. Lower guesses were associated with higher axonal density in bilateral ILF and SLF III and right SLF II and lower axonal density in the bilateral IFOF (Fig. 8a-b). These findings suggest that the "guessing" measure does not merely represent the residual noise in the behavioral responses, but rather reflects some active processes relying on long-range fibres that help reduce impacts of attentional lapses and poor task compliance. It is worth noting that the response precision, swap errors, and random guesses measures were commonly associated with $PC_4$, the axonal density in the bilateral ILF and SLF III and right SLF II, which indicates that regulating information flow in the ventral-frontoparietal-temporooccipital network might be a core mechanism underlying various visual working memory functions. This core network may closely cooperate with a supporting network, in this case, the bilateral IFOF, to form a dual system that enables more accurate, dynamic control over information processing. The IFOF has been primarily implicated in semantic language processing (Almairac et al., 2015; Martino et al., 2010). Information about task instruction might be constantly conveyed through IFOF to provide top-down modulation to the downstream areas to avoid attentional lapses and improve task compliance. This top-down signals, however, may still need to be abstract and compressed in form to preserve cognitive resources given our result that lower axonal density in the bilateral IFOF was related to fewer guesses.

The observed effects of $PC_4$, $PC_5$, and $PC_6$ did not show any notable differences between the location and orientation tasks, even though we observed robust differences between tasks when we analyzed behavioral data only. In addition, our study comprised a relatively large sample, suggesting that we should have been able to detect even small differences between tasks in brain-behavior relationship should these differences exist. The location and orientation tasks in our study involved a common encoding display but in which participants were instructed to reproduce either the spatial or non-spatial features. Previous studies using EEG recording have shown that the contralateral delay activity (CDA) tracks different features stored in visual working memory. When participants were presented with an identical array of items, greater CDA was found when participants were tested on the orientations or shapes of the items, compared with when they were tested on the colors of the items (Luria et al., 2010; Woodman and Vogel, 2008). This feature-specific difference, however, was not constrained by, or sensitive to, the axonal density in long-range white matter tracts in our study.

A strength of this study was the use of comprehensive microstructural measures across multiple tracts, utilising a data-driven approach to optimally represent spatial variations of white matter microstructure and relate this to behavior. A two-step PCA approach to the tractography data extracted six orthogonal PCs that encompassed critical information in both the measure and tract spaces. This approach addressed problems that were overlooked in previous studies investigating the relationship between visual working memory and white matter tracts. For example, Krogsrud et al. (2018) failed to find associations between visual working memory performance and the tract-based FA measures after correcting for multiple comparisons. The fact that Krogsrud et al.'s study did not replicate otherwise reproducible findings (e.g., Darki and Klingberg 2015; Nagy et al. 2004; Peters et al. 2014; Vestergaard et al. 2011; Walsh et al. 2011), raises an issue of high dimensionality in the predictor space. The use of PCA in our study aimed to achieve data reduction while providing a good representation of variation in the tractography dataset. In addition, although all studies have made claims that certain tracts are related to visual working memory, few studies have investigated the potential interactions between sets of pathways across a wider working memory network. Recent studies have argued that human cognition arises from dynamic interactions within and between large-scale functional networks (Bassett and Sporns, 2017; Bressler and Menon, 2010; Park and Friston, 2013). Structural networks comprising relatively invariant white matter fibres may also work in a collective, orchestral way as the functional networks. The two-step PCA approach in our study highlights the fact that the modulating influence of white matter microstructure goes beyond the level of individual metrics or tracts.

## 5. Conclusions

In the present study, we observed associations between visual working memory and white matter microstructure that were functionally specific to the precision of representations in visual working memory. Response precision was positively related to fibre coherence in a frontoparietal network or a frontooccipital network, depending on the level of fibre coherence in another set of tracts across the wider working memory network. We also revealed a core network for visual working memory that regulates information flow via axonal density. This core network comprises the ventral-frontoparietal-temporooccipital pathways, which together with a supporting network located elsewhere in the

brain, form a dual system for all different aspects of visual working memory responses. In summary, our study revealed both distinct and common white matter substrates for response precision, swap errors, and random guesses.

## Data availability statement

Data used in this study are available for download from the OSF repository (https://osf.io/4wkuf/).

## Funding sources

XL was supported by a scholarship from the Graduate School for Research Training, The University of Queensland. DR was supported by a National Health and Medical Research Council (Australia) Ideas grant (APP1186955). MOS was supported by a strategic award from the Deputy Vice-Chancellor for Research and Innovation, The University of Queensland. JBM was supported by a National Health and Medical Research Council (Australia) Investigator Grant (GNT2010141).

## Declaration of Competing Interest

The authors declare that there is no conflict of interests.

## Credit authorship contribution statement

**Xuqian Li:** Conceptualization, Methodology, Software, Investigation, Writing – original draft, Writing – review & editing, Visualization. **Dragan Rangelov:** Conceptualization, Methodology, Software, Writing – review & editing, Supervision. **Jason B. Mattingley:** Conceptualization, Methodology, Writing – review & editing, Supervision. **Lena Oestreich:** Methodology, Writing – review & editing. **Delphine Lévy-Bencheton:** Conceptualization, Methodology, Investigation. **Michael J. O'Sullivan:** Conceptualization, Methodology, Writing – review & editing, Supervision.

## Acknowledgments

The authors would like to thank Dr David Lloyd from the University of Queensland for his assistance with the experimental set-up.

## Supplementary materials

Supplementary material associated with this article can be found, in the online version, at doi:10.1016/j.neuroimage.2023.120069.

## References

Alexander, A.L., Lee, J.E., Lazar, M., Field, A.S., 2007. Diffusion tensor imaging of the brain. Neurotherapeutics 4 (3), 316–329. doi:10.1016/j.nurt.2007.05.011.

Alexander, D.C., Dyrby, T.B., Nilsson, M., Zhang, H., 2019. Imaging brain microstructure with diffusion MRI: practicality and applications. NMR Biomed. 32 (4), e3841. doi:10.1002/nbm.3841.

Almairac, F., Herbet, G., Moritz-Gasser, S., de Champfleur, N.M., Duffau, H., 2015. The left inferior fronto-occipital fasciculus subserves language semantics: a multilevel lesion study. Brain Struct. Funct. 220 (4), 1983–1995. doi:10.1007/s00429-014-0773-1.

Andersson, J.L.R., Sotiropoulos, S.N., 2016. An integrated approach to correction for off-resonance effects and subject movement in diffusion MR imaging. NeuroImage 125, 1063–1078. doi:10.1016/j.neuroimage.2015.10.019.

Andersson, J.L., Jenkinson, M., Smith, S., 2007. In: Non-linear registration, Aka Spatial Normalisation FMRIB Technical Report TR07JA2, 2. FMRIB Analysis Group of the University of Oxford, p. e21.

Andersson, J.L., Skare, S., Ashburner, J., 2003. How to correct susceptibility distortions in spin-echo echo-planar images: application to diffusion tensor imaging. NeuroImage 20 (2), 870–888. doi:10.1016/S1053-8119(03)00336-7.

Awh, E., Jonides, J., 2001. Overlapping mechanisms of attention and spatial working memory. Trends Cogn. Sci. 5 (3), 119–126. doi:10.1016/S1364-6613(00)01593-X, (Regul. Ed.).

Bartlett, M.S., 1951. A further note on tests of significance in factor analysis. 10.1111/j.2044-8317.1951.tb00299.x. Br. J. Stat. Psychol. 4 (1), 1–2. doi:10.1111/j.2044-8317.1951.tb00299.x.

Bassett, D.S., Sporns, O., 2017. Network neuroscience. Nat. Neurosci. 20 (3), 353–364. doi:10.1038/nn.4502.

Bates, D., Machler, M., Bolker, B.M., Walker, S.C., 2015. Fitting linear mixed-effects models using lme4. J. Stat. Softw. 67 (1), 1–48. doi:10.18637/jss.v067.i01.

Bays, P.M., 2016. Evaluating and excluding swap errors in analogue tests of working memory. Sci. Rep. 6, 19203. doi:10.1038/srep19203.

Bays, P.M., Catalao, R.F., Husain, M., 2009. The precision of visual working memory is set by allocation of a shared resource. J. Vis. 9 (10), 1–11. doi:10.1167/9.10.7, 7.

Bays, P.M., Gorgoraptis, N., Wee, N., Marshall, L., Husain, M., 2011a. Temporal dynamics of encoding, storage, and reallocation of visual working memory. J. Vis. 11 (10). doi:10.1167/11.10.6.

Bays, P.M., Wu, E.Y., Husain, M., 2011b. Storage and binding of object features in visual working memory. Neuropsychologia 49 (6), 1622–1631. doi:10.1016/j.neuropsychologia.2010.12.023.

Beaulieu, C., 2002. The basis of anisotropic water diffusion in the nervous system - a technical review. NMR Biomed. 15 (7–8), 435–455. doi:10.1002/nbm.782.

Behrens, T.E., Berg, H.J., Jbabdi, S., Rushworth, M.F., Woolrich, M.W., 2007. Probabilistic diffusion tractography with multiple fibre orientations: what can we gain? NeuroImage 34 (1), 144–155. doi:10.1016/j.neuroimage.2006.09.018.

Behrens, T.E., Woolrich, M.W., Jenkinson, M., Johansen-Berg, H., Nunes, R.G., Clare, S., Matthews, P.M., Brady, J.M., Smith, S.M., 2003. Characterization and propagation of uncertainty in diffusion-weighted MR imaging. Magn. Reson. Med. 50 (5), 1077–1088. doi:10.1002/mrm.10609.

Brainard, D.H., 1997. The psychophysics toolbox. Spat. Vis. 10 (4), 433–436. doi:10.1163/156856897X00357.

Bressler, S.L., Menon, V., 2010. Large-scale brain networks in cognition: emerging methods and principles. Trends Cogn. Sci. 14 (6), 277–290. doi:10.1016/j.tics.2010.04.004, (Regul. Ed.).

Cattell, R.B., 1966. The screen test for the number of factors. Multivariate Behav. Res. 1 (2), 245–276. doi:10.1207/s15327906mbr0102_10.

Chamberland, M., Raven, E.P., Genc, S., Duffy, K., Descoteaux, M., Parker, G.D., Tax, C.M.W., Jones, D.K., 2019. Dimensionality reduction of diffusion MRI measures for improved tractometry of the human brain. NeuroImage 200, 89–100. doi:10.1016/j.neuroimage.2019.06.020.

Clayden, J.D., Jentschke, S., Munoz, M., Cooper, J.M., Chadwick, M.J., Banks, T., Clark, C.A., Vargha-Khadem, F., 2012. Normative development of white matter tracts: similarities and differences in relation to age, gender, and intelligence. Cereb. Cortex 22 (8), 1738–1747. doi:10.1093/cercor/bhr243.

Cordero-Grande, L., Christiaens, D., Hutter, J., Price, A.N., Hajnal, J.V., 2019. Complex diffusion-weighted image estimation via matrix recovery under general noise models. NeuroImage 200, 391–404. doi:10.1016/j.neuroimage.2019.06.039.

Dagenbach, D., Munsell, B.C., Wu, G., Bonilha, L., Laurienti, P.J., 2019. Chapter 2 - insights into cognition from network science analyses of human brain functional connectivity: working memory as a test case. In: Connectomics. Academic Press, pp. 27–41. doi:10.1016/B978-0-12-813838-0.00002-9.

Daniel, T.A., Katz, J.S., Robinson, J.L., 2016. Delayed match-to-sample in working memory: a BrainMap meta-analysis. Biol. Psychol. 120, 10–20. doi:10.1016/j.biopsycho.2016.07.015.

Darki, F., Klingberg, T., 2015. The role of fronto-parietal and fronto-striatal networks in the development of working memory: a longitudinal study. Cereb. Cortex 25 (6), 1587–1595. doi:10.1093/cercor/bht352.

de Fockert, J.W., Rees, G., Frith, C.D., Lavie, N., 2001. The role of working memory in visual selective attention. Science 291 (5509), 1803. doi:10.1126/science.1056496.

de Groot, M., Vernooij, M.W., Klein, S., Ikram, M.A., Vos, F.M., Smith, S.M., Niessen, W.J., Andersson, J.L., 2013. Improving alignment in tract-based spatial statistics: evaluation and optimization of image registration. NeuroImage 76, 400–411. doi:10.1016/j.neuroimage.2013.03.015.

Düzel, E., Penny, W.D., Burgess, N., 2010. Brain oscillations and memory. Curr. Opin. Neurobiol. 20 (2), 143–149. doi:10.1016/j.conb.2010.01.004.

Dziuban, C.D., Shirkey, E.C., 1974. When is a correlation matrix appropriate for factor-analysis - decision rules. Psychol. Bull. 81 (6), 358–361. doi:10.1037/h0036316.

Emrich, S.M., Riggall, A.C., Larocque, J.J., Postle, B.R., 2013. Distributed patterns of activity in sensory cortex reflect the precision of multiple items maintained in visual short-term memory. J. Neurosci. 33 (15), 6516–6523. doi:10.1523/JNEUROSCI.5732-12.2013.

Fisher, N.I., 1995. Statistical Analysis of Circular Data. Cambridge University Press.

Forkel, S.J., Thiebaut de Schotten, M., Kawadler, J.M., Dell'Acqua, F., Danek, A., Catani, M., 2014. The anatomy of fronto-occipital connections from early blunt dissections to contemporary tractography. Cortex 56, 73–84. doi:10.1016/j.cortex.2012.09.005.

Gathercole, S.E., Pickering, S.J., Knight, C., Stegmann, Z., 2004. Working memory skills and educational attainment: evidence from national curriculum assessments at 7 and 14 years of age. Appl. Cogn. Psychol. 18 (1), 1–16. doi:10.1002/acp.934.

Geeraert, B.L., Chamberland, M., Lebel, R.M., Lebel, C., 2020. Multimodal principal component analysis to identify major features of white matter structure and links to reading. PLoS One 15 (8), e0233244. doi:10.1371/journal.pone.0233244.

Gorgoraptis, N., Catalao, R.F., Bays, P.M., Husain, M., 2011. Dynamic updating of working memory resources for visual objects. J. Neurosci. 31 (23), 8502–8511. doi:10.1523/JNEUROSCI.0208-11.2011.

Henderson, S.E., Vallejo, A.I., Ely, B.A., Kang, G., Krain Roy, A., Pine, D.S., Stern, E.R., Gabbay, V., 2014. The neural correlates of emotional face-processing in adolescent depression: a dimensional approach focusing on anhedonia and illness severity. Psychiatry Res. Neuroimaging 224 (3), 234–241. doi:10.1016/j.pscychresns.2014.09.006.

Herbet, G., Zemmoura, I., Duffau, H., 2018. Functional anatomy of the inferior longitudinal fasciculus: from historical reports to current hypotheses. Front. Neuroanat. 12 (77). doi:10.3389/fnana.2018.00077.

Hughes, J. (2021). Reghelper: helper Functions for Regression Analysis. In https://CRAN.R-project.org/package=reghelper

Isensee, J., Hucho, T., 2019. High-content imaging of immunofluorescently labeled TRPV1-positive sensory neurons. Methods Mol. Biol. 1987, 111–124. doi:10.1007/978-1-4939-9446-5_8.

Jbabdi, S., Sotiropoulos, S.N., Savio, A.M., Grana, M., Behrens, T.E., 2012. Model-based analysis of multishell diffusion MR data for tractography: how to get over fitting problems. Magn. Reson. Med. 68 (6), 1846–1855. doi:10.1002/mrm.24204.

Jenkinson, M., Bannister, P., Brady, M., Smith, S., 2002. Improved optimization for the robust and accurate linear registration and motion correction of brain images. Neuroimage 17 (2), 825–841. doi:10.1006/nimg.2002.1132.

Johnson, M.A., Diaz, M.T., Madden, D.J., 2015. Global versus tract-specific components of cerebral white matter integrity: relation to adult age and perceptual-motor speed. Brain Struct. Funct. 220 (5), 2705–2720. doi:10.1007/s00429-014-0822-9.

Kaiser, H.F., Rice, J., 1974. Little jiffy, mark 4. Educ. Psychol. Meas. 34 (1), 111–117. doi:10.1177/001316447403400115.

Krogsrud, S., Fjell, A., Tamnes, C., Grydeland, H., Due-Tønnessen, P., Bjørnerud, A., Sampaio-Baptista, C., Andersson, J., Johansen-Berg, H., Walhovd, K., 2018. Development of white matter microstructure in relation to verbal and visuospatial working memory—a longitudinal study. PLoS One 13 (4), e0195540. doi:10.1371/journal.pone.0195540.

Kucheryayskiy, S., 2020. Mdatools - R Package for Chemometrics, 198. Chemometrics and Intelligent Laboratory Systems doi:10.1016/j.chemolab.2020.103937.ARTN.103937.

Kuznetsova, A., Brockhoff, P.B., Christensen, R.H.B., 2017. lmerTest package: tests in linear mixed effects models. J. Stat. Softw. 82 (13), 1–26. doi:10.18637/jss.v082.i13.

Lazar, M., 2017. Working memory: how important is white matter? Neuroscientist 23 (2), 197–210. doi:10.1177/1073858416634298.

Luria, R., Sessa, P., Gotler, A., Jolicoeur, P., Dell'Acqua, R., 2010. Visual short-term memory capacity for simple and complex objects. J. Cogn. Neurosci. 22 (3), 496–512. doi:10.1162/jocn.2009.21214.

Maier, M.J. (.2015). Companion package to the book "R: einführung durch angewandte Statistik". In https://CRAN.R-project.org/package=REdaS

Makris, N., Kennedy, D.N., McInerney, S., Sorensen, A.G., Wang, R., Caviness, V.S., Pandya, D.N., 2005. Segmentation of subcomponents within the superior longitudinal fascicle in humans: a quantitative. In Vivo, DT-MRI Study. Cereb. Cortex 15 (6), 854–869. doi:10.1093/cercor/bhh186.

Marques, J.P., Kober, T., Krueger, G., van der Zwaag, W., Van de Moortele, P.F., Gruetter, R., 2010. MP2RAGE, a self bias-field corrected sequence for improved segmentation and T1-mapping at high field. NeuroImage 49 (2), 1271–1281. doi:10.1016/j.neuroimage.2009.10.002.

Martino, J., Brogna, C., Robles, S.G., Vergani, F., Duffau, H., 2010. Anatomic dissection of the inferior fronto-occipital fasciculus revisited in the lights of brain stimulation data. Cortex 46 (5), 691–699. doi:10.1016/j.cortex.2009.07.015.

Massey, F.J., 1951. The Kolmogorov-Smirnov test for goodness of fit. J. Am. Stat. Assoc. 46 (253), 68–78. doi:10.1080/01621459.1951.10500769.

Nagy, Z., Westerberg, H., Klingberg, T., 2004. Maturation of white matter is associated with the development of cognitive functions during childhood. J. Cogn. Neurosci. 16 (7), 1227–1233. doi:10.1162/0898929041920441.

Owen, A.M., McMillan, K.M., Laird, A.R., Bullmore, E., 2005. N-back working memory paradigm: a meta-analysis of normative functional neuroimaging studies. Hum. Brain Mapp. 25 (1), 46–59. doi:10.1002/hbm.20131.

Pajevic, S., Basser, P.J., Fields, R.D., 2014. Role of myelin plasticity in oscillations and synchrony of neuronal activity. Neuroscience 276, 135–147. doi:10.1016/j.neuroscience.2013.11.007.

Park, H.J., Friston, K., 2013. Structural and functional brain networks: from connections to cognition. Science 342 (6158), 1238411. doi:10.1126/science.1238411.

Parlatini, V., Radua, J., Dell'Acqua, F., Leslie, A., Simmons, A., Murphy, D.G., Catani, M., Thiebaut de Schotten, M., 2017. Functional segregation and integration within fronto-parietal networks. NeuroImage 146, 367–375. doi:10.1016/j.neuroimage.2016.08.031.

Pasternak, O., Sochen, N., Gur, Y., Intrator, N., Assaf, Y., 2009. Free water elimination and mapping from diffusion MRI. Magn. Reson. Med. 62 (3), 717–730. doi:10.1002/mrm.22055.

Pelli, D.G., 1997. The VideoToolbox software for visual psychophysics: transforming numbers into movies. Spat. Vis. 10 (4), 437–442. doi:10.1163/156856897X00366.

Penke, L., Munoz Maniega, S., Murray, C., Gow, A.J., Hernandez, M.C., Clayden, J.D., Starr, J.M., Wardlaw, J.M., Bastin, M.E., Deary, I.J., 2010. A general factor of brain white matter integrity predicts information processing speed in healthy older people. J. Neurosci. 30 (22), 7569–7574. doi:10.1523/JNEUROSCI.1553-10.2010.

Peters, B.D., Ikuta, T., Derosse, P., John, M., Burdick, K.E., Gruner, P., Prendergast, D.M., Szeszko, P.R., Malhotra, A.K., 2014. Age-related differences in white matter tract microstructure are associated with cognitive performance from childhood to adulthood. Biol. Psychiatry 75 (3), 248–256. doi:10.1016/j.biopsych.2013.05.020.

Pratte, M.S., Park, Y.E., Rademaker, R.L., Tong, F., 2017. Accounting for stimulus-specific variation in precision reveals a discrete capacity limit in visual working memory. J. Exp. Psychol. Hum. Percept. Perform. 43 (1), 6–17. doi:10.1037/xhp0000302.

R Core Team. *R: A Language and Environment for Statistical Computing*. In R Foundation for Statistical Computing.

Rottschy, C., Langner, R., Dogan, I., Reetz, K., Laird, A.R., Schulz, J.B., Fox, P.T., Eickhoff, S.B., 2012. Modelling neural correlates of working memory: a coordinate-based meta-analysis. NeuroImage 60 (1), 830–846. doi:10.1016/j.neuroimage.2011.11.050.

Schneegans, S., Bays, P.M., 2016. No fixed item limit in visuospatial working memory. Cortex 83, 181–193. doi:10.1016/j.cortex.2016.07.021.

Schneegans, S., Bays, P.M., 2017. Neural architecture for feature binding in visual working memory. J. Neurosci. 37 (14), 3913–3925. doi:10.1523/JNEUROSCI.3493-16.2017.

Shinoura, N., Suzuki, Y., Tsukada, M., Katsuki, S., Yamada, R., Tabei, Y., Saito, K., Yagi, K., 2007. Impairment of inferior longitudinal fasciculus plays a role in visual memory disturbance. Neurocase 13 (2), 127–130. doi:10.1080/13554790701399254.

Smith, S.M., 2002. Fast robust automated brain extraction. Hum. Brain Mapp. 17 (3), 143–155. doi:10.1002/hbm.10062.

Smith, S.M., Jenkinson, M., Woolrich, M.W., Beckmann, C.F., Behrens, T.E., Johansen-Berg, H., Bannister, P.R., De Luca, M., Drobnjak, I., Flitney, D.E., Niazy, R.K., Saunders, J., Vickers, J., Zhang, Y., De Stefano, N., Brady, J.M., Matthews, P.M., 2004. Advances in functional and structural MR image analysis and implementation as FSL. NeuroImage 23 (1), S208–S219. doi:10.1016/j.neuroimage.2004.07.051, Suppl.

Stevens, J.P., 2012. Applied Multivariate Statistics for the Social Sciences, 5th ed. Taylor & Francis.

Taylor, R., Bays, P.M., 2020. Theory of neural coding predicts an upper bound on estimates of memory variability. Psychol. Rev. 127 (5), 700–718. doi:10.1037/rev0000189.

Thiebaut de Schotten, M., Dell'Acqua, F., Forkel, S.J., Simmons, A., Vergani, F., Murphy, D.G., Catani, M., 2011. A lateralized brain network for visuospatial attention. Nat. Neurosci. 14 (10), 1245–1246. doi:10.1038/nn.2905.

Tournier, J.D., Smith, R., Raffelt, D., Tabbara, R., Dhollander, T., Pietsch, M., Christiaens, D., Jeurissen, B., Yeh, C.H., Connelly, A., 2019. MRtrix3: a fast, flexible and open software framework for medical image processing and visualisation. NeuroImage 202, 116137. doi:10.1016/j.neuroimage.2019.116137.

Veraart, J., Novikov, D.S., Christiaens, D., Ades-Aron, B., Sijbers, J., Fieremans, E., 2016. Denoising of diffusion MRI using random matrix theory. NeuroImage 142, 394–406. doi:10.1016/j.neuroimage.2016.08.016.

Vestergaard, M., Madsen, K.S., Baare, W.F., Skimminge, A., Ejersbo, L.R., Ramsoy, T.Z., Gerlach, C., Akeson, P., Paulson, O.B., Jernigan, T.L., 2011. White matter microstructure in superior longitudinal fasciculus associated with spatial working memory performance in children. J. Cogn. Neurosci. 23 (9), 2135–2146. doi:10.1162/jocn.2010.21592.

Wager, T.D., Smith, E.E., 2003. Neuroimaging studies of working memory: a meta-analysis. Cogn. Affect Behav. Neurosci. 3 (4), 255–274. doi:10.3758/cabn.3.4.255.

Walsh, M., Montojo, C.A., Sheu, Y.S., Marchette, S.A., Harrison, D.M., Newsome, S.D., Zhou, F., Shelton, A.L., Courtney, S.M., 2011. Object working memory performance depends on microstructure of the frontal-occipital fasciculus. Brain Connect 1 (4), 317–329. doi:10.1089/brain.2011.0037.

Warrington, S., Bryant, K.L., Khrapitchev, A.A., Sallet, J., Charquero-Ballester, M., Douaud, G., Jbabdi, S., Mars, R.B., Sotiropoulos, S.N., 2020. XTRACT - standardised protocols for automated tractography in the human and macaque brain. NeuroImage 217, 116923. doi:10.1016/j.neuroimage.2020.116923.

Woodman, G.F., Vogel, E.K., 2008. Selective storage and maintenance of an object's features in visual working memory. Psychon Bull. Rev. 15 (1), 223–229. doi:10.3758/PBR.15.1.223.

Yong, A.G., Pearce, S., 2013. A beginner's guide to factor analysis: focusing on exploratory factor analysis. Tutor Quant Methods Psychol. 9 (2), 79–94.

Zhang, H., Schneider, T., Wheeler-Kingshott, C.A., Alexander, D.C., 2012. NODDI: practical in vivo neurite orientation dispersion and density imaging of the human brain. NeuroImage 61 (4), 1000–1016. doi:10.1016/j.neuroimage.2012.03.072.

Zhang, W., Luck, S.J., 2008. Discrete fixed-resolution representations in visual working memory. Nature 453 (7192), 233–235. doi:10.1038/nature06860.

Zhang, Y., Brady, M., Smith, S., 2001. Segmentation of brain MR images through a hidden Markov random field model and the expectation-maximization algorithm. IEEE Trans. Med. Imaging 20 (1), 45–57. doi:10.1109/42.906424.